4 | Assembly of filamentary void galaxy configurations

We study the formation and evolution of filamentary configurations of dark matter haloes in voids. Our investigation uses the high-resolution ΛCDM simulation CosmoGrid to look for void systems resembling the VGS_31 elongated system of three interacting galaxies that was recently discovered by the Void Galaxy Survey (VGS) inside a large void in the SDSS galaxy redshift survey. HI data revealed these galaxies to be embedded in a common elongated envelope, possibly embedded in intravoid filament.

In the CosmoGrid simulation we look for systems similar to VGS_31 in mass, size and environment. We find a total of eight such systems. For these systems, we study the distribution of neighbour haloes, the assembly and evolution of the main haloes and the dynamical evolution of the haloes, as well as the evolution of the large-scale structure in which the systems are embedded. The spatial distribution of the haloes follows that of the dark matter environment.

We find that VGS_31-like systems have a large variation in formation time, having formed between 10 Gyr ago and the present epoch. However, the environments in which the systems are embedded evolved resemble each other substantially. Each of the VGS_31-like systems is embedded in an intra-void wall, that no later than $z = 0.5$ became the only prominent feature in its environment. While part of the void walls retain a rather featureless character, we find that around half of them are marked by a pronounced and rapidly evolving substructure. Five haloes find themselves in a tenuous filament of a few h^{-1}Mpc long inside the intra-void wall.

Finally, we compare the results to observed data from VGS_31. Our study implies that the VGS_31 galaxies formed in the same (proto)filament, and did not meet just recently. The diversity amongst the simulated halo systems indicates that VGS_31 may not be typical for groups of galaxies in voids.

4.1   Introduction

Voids form the most prominent aspect of the Megaparsec distribution of galaxies and matter (Chincarini and Rood 1975; Gregory and Thompson 1978; Zeldovich et al. 1982; Kirshner et al. 1981; Kirshner et al. 1987; de Lapparent et al. 1986). They are enormous regions with sizes in the range of $20 - 50 \ h^{-1}$Mpc that are practically devoid of any galaxy, usually roundish in shape and occupying the major share of volume in the Universe (see van de Weygaert and Platen 2011, for a recent review). The voids are surrounded by sheet-like walls, elongated filaments and dense compact clusters together with which they define the *Cosmic Web* (Bond et al. 1996), i.e. the salient web-like pattern given by the distribution of galaxies and matter in the Universe. Theoretical models of void formation and evolution suggest that voids act as the key organizing element for arranging matter concentrations into an all-pervasive cosmic network (Icke 1984; Regos and Geller 1991; van de Weygaert and van Kampen 1993; Sahni et al. 1994; Sheth and van de Weygaert 2004; Einasto et al. 2011; Aragon-Calvo and Szalay 2013).

Voids mark the transition scale at which density perturbations have decoupled from the Hubble flow and contracted into recognizable structural features. At any cosmic epoch, the voids that dominate the spatial matter distribution are a manifestation of the cosmic structure formation process reaching a non-linear stage of evolution. Voids emerge out of the density troughs in the primordial Gaussian field of density fluctuations. Idealized models of isolated spherically symmetric or ellipsoidal voids (Hoffman and Shaham 1982; Icke 1984; Bertschinger 1985; Blumenthal et al. 1992; Sheth and van de Weygaert 2004) illustrate how the weaker gravity in underdense regions results in an effective repulsive peculiar gravitational influence. As a result, matter is evacuating from their interior of initially underdense regions, while they expand faster than the Hubble flow of the background Universe. As the voids expand, matter gets squeezed in between them, and sheets and filaments form the void boundaries.

While idealized spherical or ellipsoidal models provide important insights into the basic dynamics and evolution of voids, computer simulations of the gravitational evolution of voids in realistic cosmological environments show a considerably more complex situation. Sheth and van de Weygaert (2004) (also see Dubinski et al. 1993; Sahni et al. 1994; Goldberg and Vogeley 2004; Furlanetto and Piran 2006; Aragon-Calvo and Szalay 2013) treated the emergence and evolution of voids within the context of *hierarchical* gravitational scenarios. It leads to a considerably modified view of the evolution of voids, in which the interaction with their surroundings forms a dominant influence. The void population in the Universe evolves hierarchically, dictated by two complementary processes. Emerging

from a primordial Gaussian field, voids are often embedded within a larger under-dense region. The smaller voids, matured at an early epoch, tend to merge with one another to form a larger void, in a process leading to ever larger voids. Some, usually smaller, voids find themselves in collapsing overdense regions and will get squeezed and demolished as they collapse with their surroundings.

A key aspect of the *hierarchical* evolution of voids is the substructure within their interior. N-body simulations show that while void substructure fades, it does not disappear (van de Weygaert and van Kampen 1993). Voids do retain a rich yet increasingly diluted and diminished infrastructure, as remnants of the earlier phases of the *void hierarchy* in which the substructure stood out more prominent. In fact, the slowing of growth of substructure in a void is quite similar to structure evolution in a low Ω Universe (Goldberg and Vogeley 2004). Structure within voids assumes a range of forms, and includes filamentary and sheet-like features as well as a population of low mass dark matter haloes and galaxies (see e.g. van de Weygaert and van Kampen 1993; Gottlöber et al. 2003). Although challenging, void substructure has also been found in the observational reality. For example, the SDSS galaxy survey has uncovered a substantial level of substructure within the Boötes void (Platen 2009), confirming tentative indications for a filamentary feature by Szomoru et al. (1996).

The most interesting denizens of voids are the rare galaxies that populate these underdense region, the *void galaxies* (Szomoru et al. 1996; Kuhn et al. 1997; Popescu et al. 1997; Karachentseva et al. 1999; Grogin and Geller 1999, 2000; Hoyle and Vogeley 2002, 2004; Rojas et al. 2004, 2005; Tikhonov and Karachentsev 2006; Patiri et al. 2006a,b; Ceccarelli et al. 2006; Park et al. 2007; von Benda-Beckmann and Müller 2008; Wegner and Grogin 2008; Stanonik et al. 2009; Kreckel et al. 2011; Pustilnik and Tepliakova 2011; Kreckel et al. 2012; Hoyle et al. 2012). The relation between void galaxies and their surroundings forms an important aspect of the recent interest in environmental influences on galaxy formation. Void galaxies appear to have significantly different properties than average field galaxies. They appear to reside in a more youthful state of star formation and possess larger and less distorted gas reservoirs. Analysis of void galaxies in the SDSS and Two-degree-Field Galaxy Redshift Survey (2dFGRS) indicate that void galaxies are bluer and have higher specific star formation rates than galaxies in denser environments.

4.1.1 The Void Galaxy Survey

A major systematic study of void galaxies is the Void Galaxy Survey (VGS), a multi-wavelength program to study ∼60 void galaxies selected from the SDSS DR7 redshift survey (Stanonik et al. 2009; Kreckel et al. 2011, 2012). These galax-ies were selected from the deepest inner regions of voids, with no a priori bias on

the basis of the intrinsic properties of the void galaxies. The voids were identified using of a unique geometric technique, involving the Watershed Void Finder (Platen et al. 2007) applied to a Delaunay Tesselation Field Estimator (DTFE) density field reconstruction. An important part of the program concerns the gas content of the void galaxies, and thus far the HI structure of 55 VGS galaxies has been mapped. In addition, it also involves deep B and R imaging of all galaxies, Hα and GALEX UV data for assessing the star formation properties of the void galaxies.

Perhaps the most interesting configuration found by the Void Galaxy Survey is VGS_31 (Beygu et al. 2013). Embedded in an elongated common HI cloud, at least three galaxies find themselves in a filamentary arrangement with a size of a few hundred kpc. One of these objects is a Markarian galaxy, showing evidence for recent accretion of minor galaxies. Along with the central galaxy, which shows strong signs of recent interaction, there is also a starburst galaxy.

We suspect, from assessing the structure of the void, that the gaseous VGS_31 filament is affiliated to a larger filamentary configuration running across the void and visible at one of the boundaries of the void. This elicits the impression that VGS_31 represents a rare specimen of a high density spot in a tenuous dark matter void filament. Given the slower rate of evolution in voids, it may mean that we find ourselves in the unique situation of witnessing the recent assembly of a filamentary galaxy group, a characteristic stage in the galaxy and structure formation process.

4.1.2   Outline

In this study we concentrate on implications of the unique VGS_31 configuration for our understanding of the dynamical evolution of void filaments and their galaxy population. We are interested in the assembly of the filament configuration itself, as well as that of the halo population in its realm. In fact, we use the specific characteristics of the VGS_31 galaxies, roughly translated from galaxy to dark matter halo, to search for similar dark halo configurations in the CosmoGrid simulation (Portegies Zwart et al. 2010a; Ishiyama et al. 2013, see Figure 4.1).

Subsequently, we study in detail the formation and evolution of the entire environment of these haloes. In this way, we address a range of questions. What has been the assembly and merging history of the configuration? Did the VGS_31 galaxies recently meet up and assemble into a filament, or have they always been together? Is the filament an old feature, or did it emerge only recently? May we suspect the presence of more light mass galaxies in the immediate surrounding of VGS_31, or should we not expect more than three such galaxies in the desolate void region?

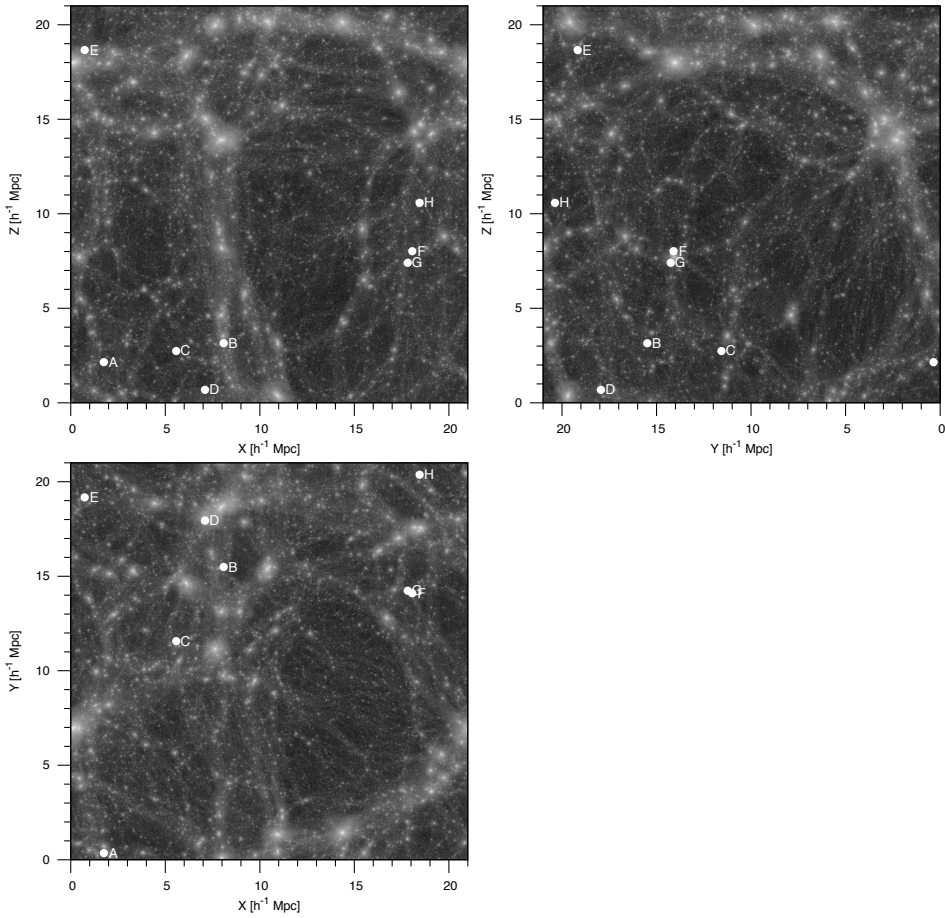Our study uses a pure dark matter N-body simulation. While a full under-

Figure 4.1: A snapshot of the full CosmoGrid volume seen from different sides, with dots indicating the locations of the void halo systems. The images display the full $(21\ h^{-1}\mathrm{Mpc})^3$ volume.

standing of the unique properties of VGS_31 evidently should involve the complexities of its gas dynamical history, along with that of the stellar populations, here we specifically concentrate on the overall gravitational aspects of its dynamical evolution. The reason for this is that the overall evolution of the filamentary structure will be dictated by the gravitational influence of the mass concentrations in and around the void. For a proper understanding of the context in which VGS_31 may have formed, it is therefore better to concentrate solely on the gravitational evolution.

The outline of this paper is as follows. In section 4.2.1, we discuss the simulation used in this article, along with the criteria which we used for the selecting VGS-31 resembling halo configurations. The properties and evolution of the eight selected halo groups are presented and discussed in section 4.3. Section 4.4 continues the discussion by assessing the large scale environment in which the VGS_31 resembling configurations are situated, with special attention to the walls and filaments in which they reside. We also investigate the evolution of the surrounding filamentary pattern as the haloes emerge and evolve. Finally, in section 4.5 we evaluate and discuss the most likely scenario for the formation of void systems like VGS_31. In section 4.6 we summarize and discuss our findings.

4.2   Simulations

4.2.1   Setup

In order to evaluate possible formation scenarios for systems like VGS_31, we investigate the formation of systems with similar properties in a cosmological simulation. For this purpose, we use the CosmoGrid ΛCDM simulation (Ishiyama et al. 2013). The CosmoGrid simulation contains 2048^3 particles within a volume of 21 $h^{-1}\mathrm{Mpc}^3$, and has high enough mass resolution (8.9×10^4 $h^{-1}\mathrm{M}_\odot$ per particle) to study both dark matter haloes and the dark environment in which the haloes form. The CosmoGrid simulation used a gravitational softening length ϵ of 175 parsec, and the following cosmological parameters: $\Omega_m = 0.3, \Omega_\Lambda = 0.7, h = 0.7, \sigma_8 = 0.8$ and $n = 1.0$.

The first reduction step concerns the detection and identification of haloes and their properties in the CosmoGrid simulation. For this, we use the `Rockstar` halo finder. Rockstar uses a six-dimensional friends-of-friends algorithm to detect haloes in phase-space. It excels in tracking substructure, even in ongoing major mergers and in halo centres (e.g. Knebe et al. 2011; Onions et al. 2012).

Since we are interested in the formation history of the haloes, we analyse multiple snapshots. Merger trees are constructed to identify haloes across the snapshots,
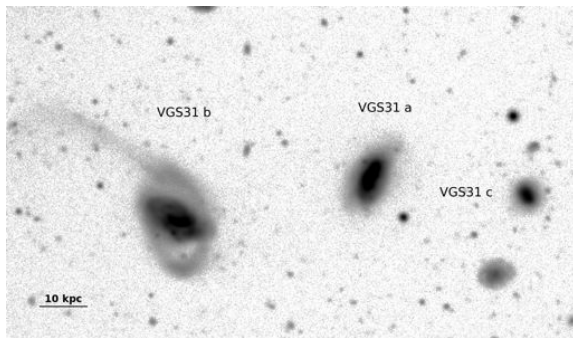
Figure 4.2: B band image of the VGS_31 system: VGS_31_b (left), VGS_31_a (centre) and VGS_31_c (right). The physical scale of the system may be inferred from the bar in the lower left-hand corner.

for which we use the gravitationally consistent merger tree code from Behroozi et al. (2013b). For this we use 193 CosmoGrid snapshots, equally spaced in time at 70 Myr intervals.

Finally, to compare the CosmoGrid haloes to the galaxies observed in void regions, we need to identify the regions in CosmoGrid that can be classified as voids. In doing so we compute the density field using the Delaunay Tessellation Field Estimator (DTFE, Schaap and van de Weygaert 2000; van de Weygaert and Schaap 2009; Cautun and van de Weygaert 2011). We express the resulting density in units of the mean background density $< \rho >$ as $1 + \delta = \rho / < \rho >$. The resulting density field is smoothed with $1\ h^{-1}$Mpc Gaussian filter to obtain a large scale density field. We identify voids as the regions with a $1\ h^{-1}$Mpc smoothed density contrast of $\delta < -0.5$.

4.2.2   Selection of the simulated haloes

The VGS_31 system consists of three galaxies with spectrophotometric redshift $z = 0.0209$. The principal galaxies VGS_31a and VGS_31b, and the 2 magnitudes fainter galaxy VGS_31c, are stretched along an elongated configuration of ~ 120 kpc in size (see Figure 4.2). The properties of the VGS_31 galaxies are listed in Table 4.1. The three galaxies are connected by an HI bridge that forms a filamentary structure in the void (Beygu et al. 2013). Both VGS_31a and VGS_31b show strong signs of tidal interactions. VGS_31b has a tidal tail and a ring like structure wrapped around the disk. This structure can be the result of mutual gravitational interaction with VGS_31a or may be caused by a fourth object that fell in VGS_31b.

We use the CosmoGrid simulation to select halo configurations that resemble VGS_31. In doing so we define a set of five criteria that the halo configuration should fulfil at $z = 0$. The first two criteria involve the properties of individual haloes:
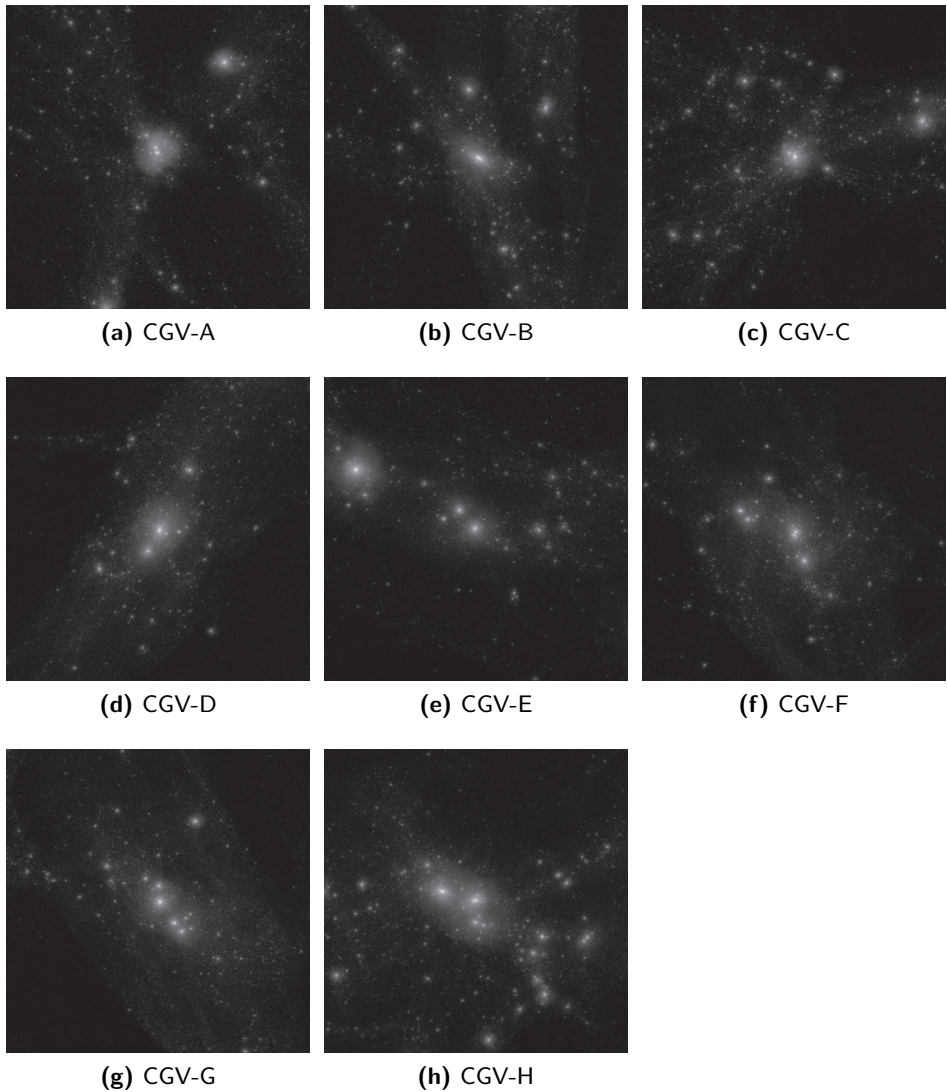
(a) CGV-A   (b) CGV-B   (c) CGV-C

(d) CGV-D   (e) CGV-E   (f) CGV-F

(g) CGV-G   (h) CGV-H

Figure 4.3: CosmoGrid Void systems A - H. The frames show the dark matter density distri-
bution in regions of $1\ h^{-1}\mathrm{Mpc}^3$ around the principal haloes of each CGV system.

Table 4.1: Some of the properties of VGS_31 member galaxies.

Name	M_*	M_{HI}	M_{dyn}	δ
	$10^8 M_\odot$	$10^8 M_\odot$	$10^{10} M_\odot$	
(1)	(2)	(3)	(4)	(5)
VGS_31a	35.1	19.89 ± 2.9	< 2.31	-0.64
VGS_31b	105.31	14.63 ± 1.97		
VGS_31c	2.92	1.66 ± 0.95		

Object name (1). Stellar mass (2). HI mass (3). Dynamic mass (4). Density contrast after applying a $1\ h^{-1}$Mpc Gaussian filter (5).

- We select only haloes with mass M_{vir} in the range $2 \times 10^{10}\ h^{-1}\text{M}_\odot$ to $10^{11}\ h^{-1}\text{M}_\odot$. This represents a reasonable estimate for the mass of the most massive dark matter halo in the VGS_31 system.

- Out of the haloes found above, we keep only the ones which reside in void-like region, where the $1\ h^{-1}$Mpc smoothed density fulfils $\delta \leqslant -0.50$.

There are 84 haloes in the CosmoGrid simulation that fulfil the above two criteria. Subsequently, we further restrict the selection to those haloes that are located within a system that is similar to VGS_31. To that end, we look at the properties of all haloes and subhaloes within a distance of $200\ h^{-1}$kpc from the main haloes selected above. A system is selected when the primary halo has, within $200\ h^{-1}$kpc:

- a secondary (sub)halo with $M_{\text{vir}} > 5 \times 10^9\ h^{-1}\text{M}_\odot$,

- a tertiary (sub)halo with $M_{\text{vir}} > 10^9\ h^{-1}\text{M}_\odot$,

- no more than 5 neighbour (sub)haloes with $M_{\text{vir}} > 5 \times 10^9\ h^{-1}\text{M}_\odot$.

Following the application of these criteria, we find a total of 8 VGS_31-like systems in the CosmoGrid simulation. We call these systems the CosmoGrid Void systems. The individual haloes in the eight void halo systems are indicated by means of a letter, eg. CGV-A_a and CGV-A_b. In the subsequent sections we investigate the halo evolution, merger history and large scale environment of the eight void halo configurations.

4.2.3   Analysis of the environment

We investigate the formation and evolution of the eight CGVs within the context of the large scale environment in which they reside. In doing so we use the NEXUS+ method (Cautun et al. 2013) to identify the morphology of large scale

Table 4.2: Properties of the eight CosmoGrid Void systems found to resemble VGS_31.

Name	M_{vir} $10^{10}\,h^{-1}M_\odot$	R_{vir} h^{-1}kpc	V_{max} km/s	r h^{-1}kpc	θ °	ϕ °	δ	last MM Gyr	$\angle_{wall}$ °	$\angle_{fil}$ °
(1)	(2)	(3)	(4)	(5)	(6)	(7)	(8)	(9)	(10)	(11)
CGV-A_a	3.15	64.5	48.7				-0.68	-	51.45	-
CGV-A_b	0.59	36.8	34.6	17	94.0	111.2	-0.68		12.48	-
CGV-A_c	0.16	23.9	22.1	76	61.9	122.6	-0.68		59.24	-
CGV-B_a	3.95	69.5	63.5				-0.51	5.24	20.80	80.71
CGV-B_b	0.87	42.0	47.6	23	20.1	141.5	-0.51		46.76	62.02
CGV-B_c	0.16	23.7	29.8	20	26.9	135.8	-0.51		17.04	86.71
CGV-C_a	2.99	63.3	54.8				-0.51	1.19	11.94	-
CGV-C_b	0.54	35.8	34.0	37	36.1	142.7	-0.51		34.79	-
CGV-C_c	0.14	23.0	24.2	64	2.9	81.4	-0.51		5.49	-
CGV-C_d	0.13	22.3	22.6	113	93.4	-19.5	-0.51		82.73	-
CGV-D_a	4.60	73.1	61.3				-0.63	10.9	23.18	20.41
CGV-D_b	0.93	42.9	38.9	86	114.0	-119.2	-0.63		2.36	55.11
CGV-D_c	0.16	23.6	30.7	71	65.9	-4.1	-0.63		40.89	62.16
CGV-D_d	0.13	22.3	24.1	32	52.7	-25.2	-0.63		18.54	86.89
CGV-E_a	1.99	55.3	54.4				-0.57	2.44	8.54	30.67
CGV-E_b	1.01	44.1	44.7	82	104.9	130.1	-0.57		68.28	85.00
CGV-E_c	0.23	26.8	33.5	120	115.7	162.7	-0.57		72.48	81.23
CGV-F_a	2.27	57.8	55.0				-0.62	-	49.25	73.83
CGV-F_b	0.74	39.8	40.1	14	124.3	-119.7	-0.62		77.65	89.75
CGV-F_c	0.11	21.2	28.9	6	169.6	-101.4	-0.62		63.99	82.47
CGV-G_a	2.14	56.7	57.4				-0.61	5.80	4.26	12.07
CGV-G_b	0.93	42.9	47.8	139	37.2	-55.6	-0.61		20.95	34.20
CGV-G_c	0.38	31.8	34.4	74	45.3	94.0	-0.61		18.27	15.73
CGV-H_a	4.63	73.3	66.0				-0.50	8.45	4.01	-
CGV-H_b	4.69	73.6	68.7	199	145.5	164.4	-0.50		17.65	-
CGV-H_c	0.69	38.8	38.0	153	151.8	-89.4	-0.50		8.84	-
CGV-H_d	0.28	28.6	28.4	92	111.7	-71.6	-0.50		43.94	-
CGV-H_e	0.10	20.6	27.9	33	147.3	67.0	-0.50		67.46	-
CGV-H_f	0.10	20.5	22.7	86	142.1	-76.8	-0.50		54.10	-

Object name (1). Virial mass (2). Virial radius (3). Maximum rotational velocity (4). Position relative to most massive system (5,6,7). Density contrast at halo position (smoothed with $1\ h^{-1}$Mpc Gaussian filter) (8). Time at which the last major merger took place (9). Angle between the angular momentum axis of the halo and the normal of the wall (10). Angle between the angular momentum axis of the halo and the filament. (11)
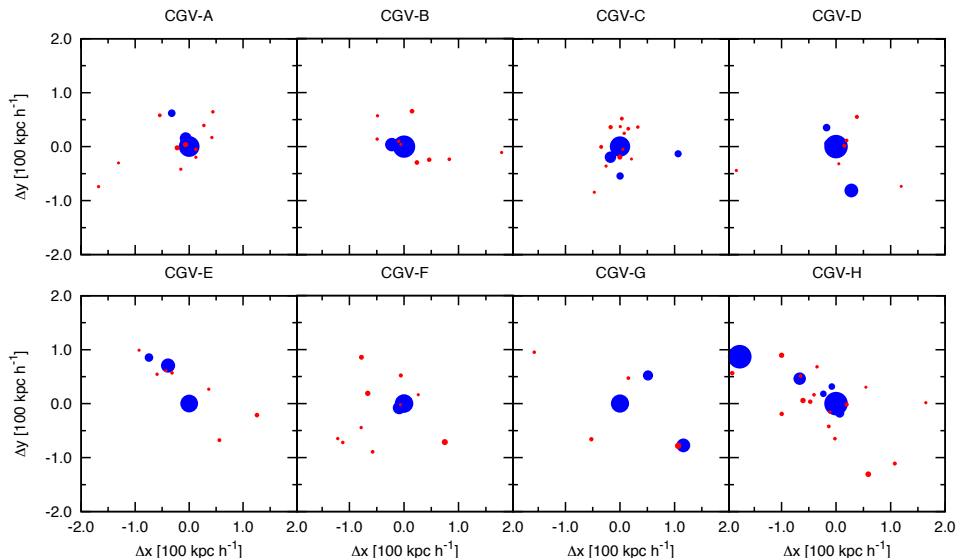
Figure 4.4: The spatial distribution of the haloes and subhaloes in the eight CGVs. The blue points show objects more massive than $10^9\ h^{-1}\mathrm{M}_\odot$, with point sizes proportional to halo mass. Red points show haloes and subhaloes in the mass range $(0.1-1) \times 10^9\ h^{-1}\mathrm{M}_\odot$. The plane of the projection is along the large scale wall in which these systems are embedded.

structure around the selected haloes. At each location within the simulation box, it determines whether it belongs to a void or field region, a wall, a filament or a dense cluster node.

The NEXUS+ algorithm is a multiscale formalism that assigns the local morphology on the basis of a scale-space analysis. It is an elaboration and extension of the MMF algorithm introduced by Aragón-Calvo et al. (2007). It translates a given density field into a scale-space representation by smoothing the field on a range of scales. The morphology signature at each of the scales is inferred from the eigenvalues of the Hessian of the density field. The final morphology is determined by selecting the scale which yields the maximum signature value. To discard spurious detections, we use a set of physical criteria to set thresholds for significant morphology signatures.

For a detailed description of the NEXUS+ algorithm, along with a comparison with other Cosmic Web detection algorithms, we refer to Cautun et al. (2013). The method involves the following sequel of key steps:

1. Application of the Log-Gaussian filter of width R_n to the density field.

2. Calculation of the Hessian matrix eigenvalues for the filtered density field.

3. Assigning to each point a cluster, filament and wall signature on the basis of the three Hessian eigenvalues computed in the previous step.

4. Repetition of steps *(i)* to *(iii)* over a range of smoothing scales $(R_0, R_1, \ldots, R_N)$. For this analysis we filter from $R_0 = 0.1\ h^{-1}\mathrm{Mpc}$ to $4\ h^{-1}\mathrm{Mpc}$, in steps $R_n = R_0 2^{n/2}$.

5. Combination of the morphology signatures at each scale to determine the final scale independent cluster, filament and wall signature.

6. Physical criteria are used to set detection thresholds for significant values of the morphology signatures.

Two important characteristics of NEXUS+ makes it the ideal tool for studying filamentary and wall-like structures in lower density regions. First of all, NEXUS+ is a scale independent method which means that it has the same detection sensitivity for both large and thin filaments and walls. And secondly, Cautun et al. (2013) showed that the method picks up even the more tenuous structures that permeate the voids. Usually these structures have smaller densities and are less pronounced than the more massive filaments and walls, but locally they still have a high contrast with respect to the background and serve as pathways for emptying the voids. Both of these two strengths are crucial for this work since the CGV haloes populate void-like regions with very thin and tenuous filaments and walls.

4.3   Evolution of void haloes

In the CosmoGrid simulation we find a total of eight systems (see Figure 4.3) adhering to the search parameters specified in section 4.2.2. We label these CGVs A to H. These systems contains from 3 up to 6 haloes with masses larger than $10^9\ \mathrm{M}_\odot$. They are labelled by an underscore letter, eg. CGV-H_a or CGV-H_f. In Figure 4.1, we show the locations of these systems in three mutually perpendicular projections of the $21\ h^{-1}\mathrm{Mpc}$ CosmoGrid box. Figure 4.3 further zooms in on the structure of these systems by showing the density distribution in boxes of $1\ h^{-1}\mathrm{Mpc}$ surrounding the eight configurations.

At z=0, the CGV haloes have a similar appearance. Within a radius of $500\ h^{-1}\mathrm{kpc}$, the primary halo of most of the systems is the largest object. The exceptions are the CGV-E and CGV-H systems, which have a larger neighbouring halo. The general properties of the CGVs are listed in Table 4.2.

Figure 4.4 provides an impression of the spatial distribution of the haloes in these eight CVG systems. The principal haloes, those with a mass in excess of $10^9\ \mathrm{M}_\odot$, are represented by a blue dot whose size is proportional to its mass. They
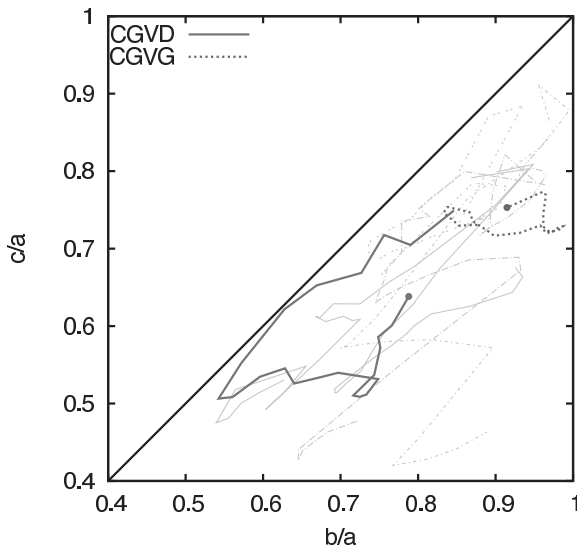
Figure 4.5: Shape of the primary CGV haloes, CGV-A_a to CGV-G_a. Each track represents the change in the shape of the halo with distance from the halo centre, out to the virial radius (indicated with a dot). We distinguish three interesting regions in the plot: top right ($a \approx b \approx c$, i.e. $c/a = b/a = 1$) indicates a spherical halo, bottom left ($a > b \approx c$, ie. $c/a \approx b/a$) indicates a stretched halo (cigar shaped), bottom right ($a \approx b \gg c$, ie. $c/a \ll b/a = 1$) indicates a flattened halo. We emphasize the tracks for CGV-D_a (solid) and CGV-G_a (dashed).
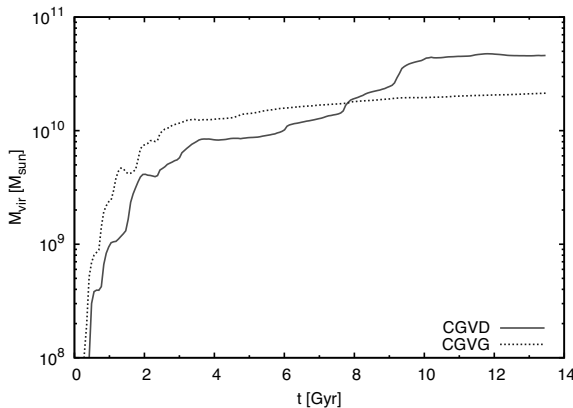
Figure 4.6: Mass accretion history for two selected haloes, CGV-D_a (solid) and CGV-G_a (dashed). The plot gives the mass contained within each halo as a function of time. CGV-D_a is marked by three sudden major mass accretions after $t = 4$ Gyr, while CGV-G_a leads a quiescent life after it experience an early major merger at $t = 2.5$ Gyr.

are the haloes listed in Table 4.2. In addition, we plot the location of surrounding small haloes with a mass in the range of $10^8 < M < 10^9$ M$_\odot$. While there are substantial differences between the small-scale details of the mass distribution, we can recognize the global aspect of a filamentary arrangement of a few dominant haloes that characterizes VGS_31. This is particularly clear for the systems CGV-D, CGV-E, CGV-G and CGV-H.

4.3.1   Halo Structure

To investigate the shape characteristics of the principal haloes, we evaluate the shape of their mass distribution as a function of radius. To this end, we measure the

principal axis ratios of the mass distribution contained within a given radius. These are obtained from the moment of inertia tensor for the mass contained within that radius. In Figure 4.5 we plot the resulting run of shape - characterized by the two axis ratios b/a and c/a, where $a \geqslant b \geqslant c$ - for a range of radii smaller than the virial radius, $r < R_{\mathrm{vir}}$. Spherical haloes would be found in the top right-hand of the figure, with $b/a \approx c/a \approx 1$. Haloes at the bottom left-hand corner, where $c \approx b \ll a$, resemble elongated spindles while those at the bottom right-hand corner, with $c \ll b \approx a$, have a flattened shape.

Each halo is represented by a trail through the shape diagram, with each point on the trail representing the shape of the halo at one particular radius. Figure 4.5 emphasizes the trails of CGV-D_a (solid) and CGV-G_a (dashed), while the results for the remaining six haloes are presented in grey. The shape of the quiescently evolving CGV-G_a halo tends towards a near-spherical shape, as one may expect (Araya-Melo et al. 2009). By contrast, the strongly evolving primary CGV-D_a halo has a strongly varying shape. In the centre and near the virial radius it is largely spherical, while in between it is more stretched.

4.3.2   Halo Assembly and Evolution

Using the merger trees of the primary CGV haloes, we investigate the evolution and assembly history of the eight systems.

We find that only the CGV-D and CGV-H systems experienced major mergers in the last half Hubble time, the other systems undergoing only smaller mergers. From the CGVs we select the two most extreme cases that we study in more detail: CGV-D as a recently formed system and CGV-G as a system that formed very early on. The primary halo of the CGV-D system (CGV-D_a) formed at a very late moment from many similar-sized progenitors. It only appears as the dominant halo around $t = 10$ Gyr, when it experiences its last big merger event. By contrast, the central CGV-G halo (CGV-G_a) formed much earlier, and did not experience any significant merger after $t = 5.5$ Gyr.

In Figure 4.6, we show the mass accretion history of the primary haloes of both systems. After $t = 4$ Gyr, CGV-D_a shows sudden, major accretions of mass on three occasions, at $t = 6$, 7.7 and 9.2 Gyr. This halo reached 50% of its final virial mass only at $t = 8.8$ Gyr. CGV-G_a, on the other hand, had already reached 50% of its virial mass at $t = 2.5$ Gyr and does not show any large increases of mass after $t = 4$ Gyr.

The detailed merger histories of systems CGV-D and CGV-G - limited to haloes larger than $5 \times 10^7 \ h^{-1} \mathrm{M}_\odot$ - are shown in Figure 4.7. The figure depicts the merger tree, along with a corresponding sequence of visual images of the assembly of these systems.

The sequence of images from Figure 4.7 suggests that the assembly takes place within a spatial configuration of hierarchically evolving filamentary structures. For both systems, the many filaments that are clearly visible in the first snapshot merge into a single, thicker filament by the second snapshot. As the system evolves, it collects most of the mass from the filament as it gets accreted onto the haloes. We analyse this in more detail in section 4.4.

4.3.3   Dynamical Evolution

We use the dominant mass concentrations in each CGV to get an impression of the global evolution of the mass distribution around the central halo. Using the merger tree of each void halo configuration, we obtain the location of the main and secondary halo for each of the CGVs. To assess the overall dynamics, we first look at the physical dimension of the emerging systems. Figure 4.8 shows the physical distance between the main and secondary halo of each system. In all cases we see the typical development of an overdense region: a gradual slow-down of the cosmic expansion, followed by a turnaround into a contraction and collapse. We find that the average physical distance between the main and secondary haloes increases from about 100 kpc at $t = 1$ Gyr to 200 kpc at $t = 6$ Gyr. Subsequently, the systems start to contract to 100 kpc at $t = 13.5$ Gyr. The exceptions are CGV-H and CGV-G, and as well CGV-E and CGV-F. CGV-E and CGV-F display more erratic behaviour. For a long timespan, CVG-E hovers around the same physical size, turning around only at $t \approx 9$ Gyr. To a large extent, this is determined by the dominant external mass concentration in the vicinity of CGV-E. Even more deviant is the evolution of CGV-F, where we distinguish an early and a later period of recession and approach between the principal and secondary halo. It is a reflection of a sequence of mergers, in which the two principal haloes at an early time merged into a halo which subsequently started its approach towards a third halo.

The corresponding evolution of the co-moving distance between the two main haloes of each CGV provides complementary information on their dynamical evolution. The evolving co-moving distance is plotted in Figure 4.9. Evidently, each of these overdense void halo systems is contracting in co-moving space. We find that the distance between main and secondary halo decreases from about $400 - 600 \ h^{-1}$kpc at $t = 1$ Gyr to its current value at $z = 0$ of less than $200 \ h^{-1}$kpc. CGV-G, CGV-E and CGV-F have a markedly different history than the others. A rapid decline at early times is followed by a shallow decline over the last 10 Gyr. It is the reflection of an early merger of haloes, followed by a more quiescent period in which the merged haloes gradually move towards a third halo.
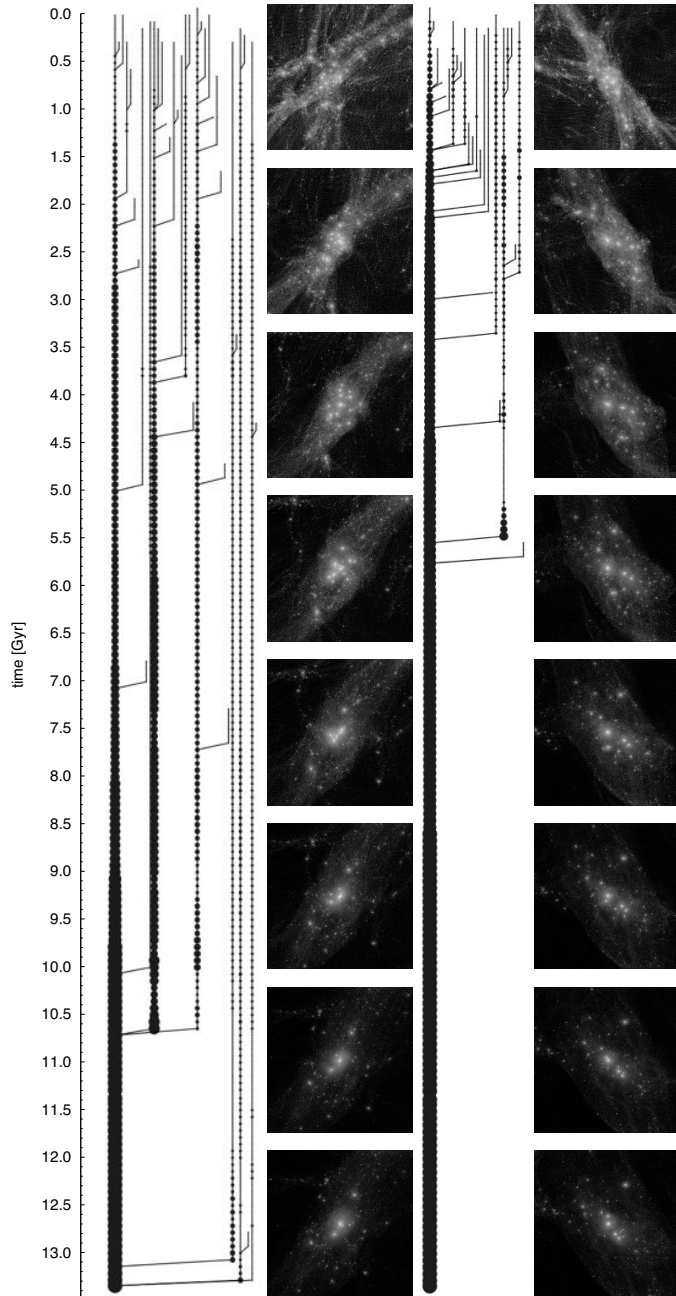
Figure 4.7: The merger history of the central haloes of CGV-D (left) and CGV-G (right). The size of the filled circles is proportional to the virial mass of the halo. We show only haloes and subhaloes with a peak mass larger than $5 \times 10^7 \ h^{-1} \mathrm{M}_\odot$ that are accreted before $z = 0$. Halo D had a violent merger history, originating from many smaller systems, whereas halo G has remained virtually unchanged since very early in its history.
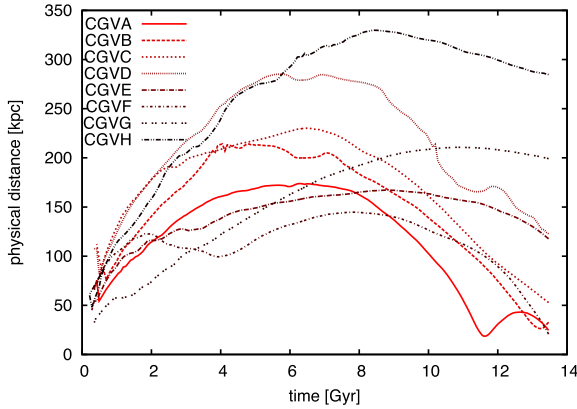
Figure 4.8: The relative physical distance between the main and secondary haloes for each of the eight CGVs. Plotted is physical distance, in kpc, as a function of cosmic time (Gyr).
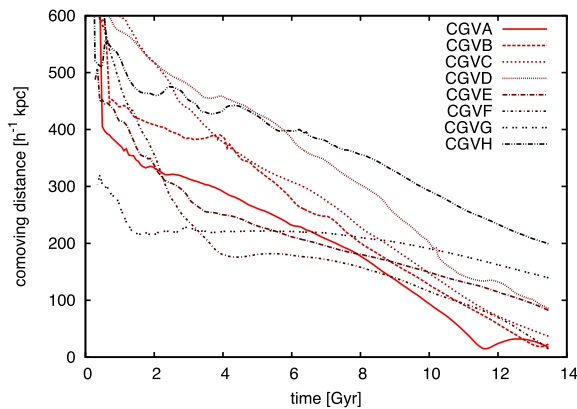
Figure 4.9: The relative co-moving distance between the main and secondary haloes for each of the eight CGVs. Plotted is co-moving distance, in kpc, as a function of cosmic time (Gyr).

4.4   Large scale environment

The various VGS_31 resembling halo configurations are embedded in either walls or filaments within the interior of a void. For our study, it is therefore of particular interest to investigate the nature of the large-scale filamentary and planar features in which the CGVs reside.

We first look at the specific structural environment of one particular CGV complex, CGV-G. Subsequently, we inspect the generic structural morphology of the mass and halo distribution around the CGVs. Finally, we assess the dynamical evolution of the anisotropic mass distribution around the CGVs.

4.4.1   The web-like environment of CGV-G

The mass distribution within a 7 h^{-1}Mpc box around the CGV-G halo complex is shown in Figure 4.10. It depicts the projected mass distribution along three mutually perpendicular planes. It includes a 1 h^{-1}Mpc sized zoom-in, in the XY plane, onto the halo complex.

The global structure of the mass distribution is that of a wall extending over the YZ plane. In the XY- and XZ-projections, the wall is seen edge-on. They convey the impression of the coherent nature of the wall, in particular along the ridge in the Z-direction. This is confirmed by the NEXUS+ analysis of the morphological nature of the mass distribution, presented in Figure 4.11. At the current epoch we clearly distinguish a prominent wall-like structure (dark grey, lower central frame). Within the plane of the wall, the halo - indicated by a white dot - is located in a filament (light grey, lower right-hand frame). These findings suggest that in the immediate vicinity of the CGVs we should expect haloes to be aligned along the filament.

The filamentary nature of the immediate halo environment may also be inferred from the pattern seen in the Mollweide sky projection of the surrounding dark matter distribution. Figure 4.12 shows this for the dark matter distribution around CGV-G out to a radius of 1 h^{-1}Mpc. At $z = 0$, the angular distribution is marked by the typical signature of a filament (lower right-hand frame): two high density spots at diametrically opposite locations. These spots indicate the angular direction of the filament in which CGV-G is embedded. In the same figure, we also follow the sky distribution for the CGV-D halo (lower left-hand frame). A similar pattern is seen for this halo, although its embedding filament appears to be more tenuous and has a lower density.
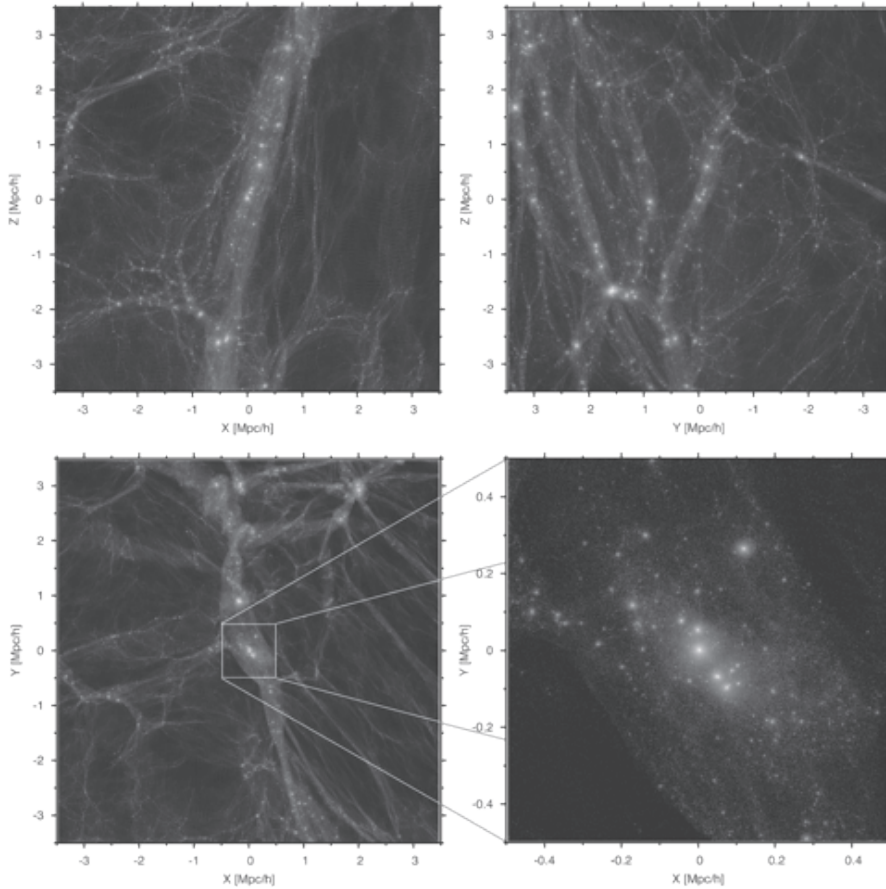
Figure 4.10: CGV-G and its large-scale void environment. Each of the frames shows the projected density distribution, within a $1\ h^{-1}\mathrm{Mpc}$ thick slice in a $7\ h^{-1}\mathrm{Mpc}$ wide region around CGV-G. Top left: XZ plane; top right: YZ plane; bottom left: XY plane. Bottom right: a $1\ h^{-1}\mathrm{Mpc}$ wide zoom-in onto the XY plane, centred on CGV-G. Particularly noteworthy is the pattern of largely aligned tenuous intravoid filaments in the YZ plane.
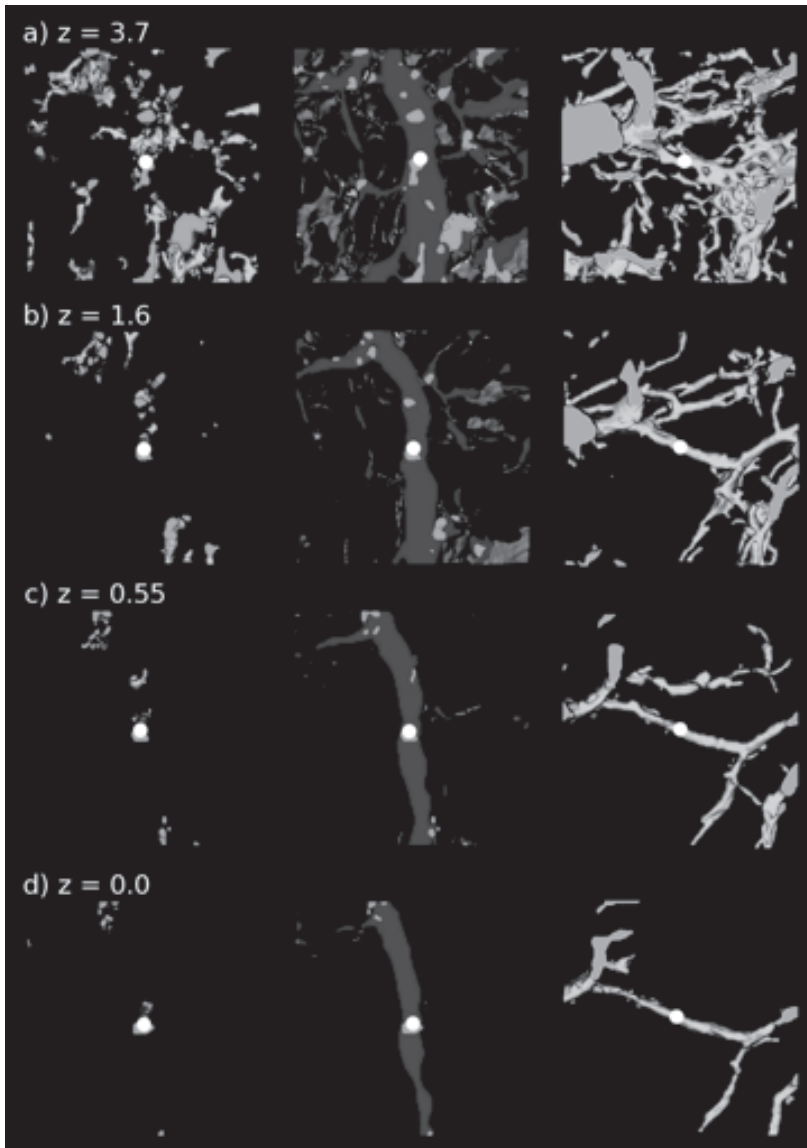
Figure 4.11: The evolution of the morphology of the mass distribution around the central halo of CGV-G. The wall-like (dark grey) and filamentary (light grey) features have been identified with the help of NEXUS+ . The frames show the features in a box of $5~h^{-1}\mathrm{Mpc}$ (co-moving) size and $1~h^{-1}\mathrm{Mpc}$ thickness. Within each frame the location of CGV-G_a is indicated by a white dot. The figure shows the evolution of the morphological features at four redshifts: $z = 3.7, z = 1.6, z = 0.55$ and $z = 0.0$. The first two columns correspond to edge-on orientations of the wall, with the leftmost ones showing the filamentary evolution along the wall and the central one that of the evolution of the wall-like features. The right-hand column depicts the evolution of the filamentary structures within the plane of the wall.
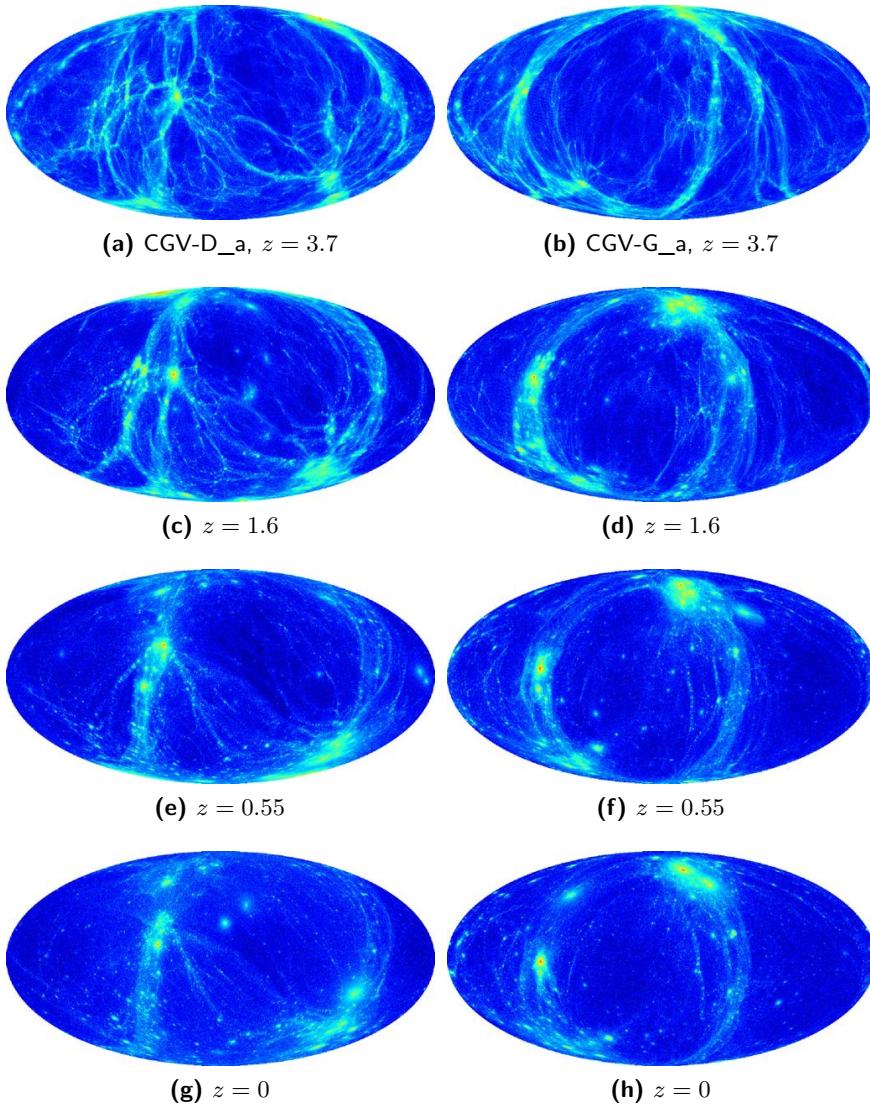
(a) CGV-D_a, $z = 3.7$

(b) CGV-G_a, $z = 3.7$

(c) $z = 1.6$

(d) $z = 1.6$

(e) $z = 0.55$

(f) $z = 0.55$

(g) $z = 0$

(h) $z = 0$

Figure 4.12: Mollweide projection of the angular dark matter density distribution around haloes CGV-D_a (left) and CGV-G_a (right). To obtain the sky density we projected the dark matter density within a distance of $1\ h^{-1}\mathrm{Mpc}$ from the primary halo centre. The figure depicts the evolution of the sky density at four redshifts: $z = 3.7, z = 1.6, z = 0.55$ and $z = 0$. The signature of a wall-like configuration is a circular mass arrangement over the sky, that of a filamentary structure consist of two dense spots at diametrically opposite angular positions. In the case of both CGV-D and CGV-G, the evolution towards a wall with an intersecting filament at $z = 0$ is clearly visible. Dark blue areas correspond to a mass count $< 10^5\ h^{-1}\mathrm{M}_\odot$, whereas red areas correspond to a mass count $> 10^{10}\ h^{-1}\mathrm{M}_\odot$.
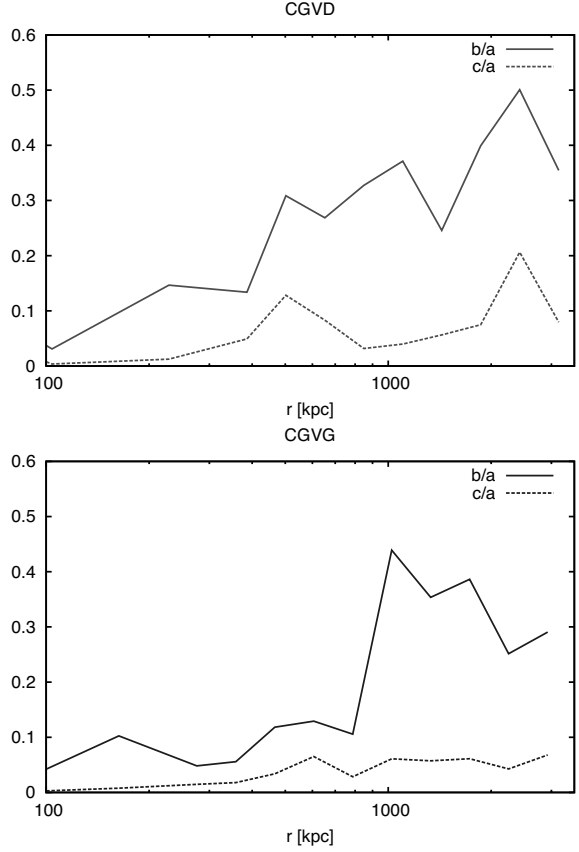
Figure 4.13: Shape of the neighbour halo distribution for central haloes CGV-D_a (top) and CGV-G_a (bottom) (haloes included have a mass $M_{\mathrm{vir}} > 10^8\ h^{-1}\mathrm{M}_\odot$). The shape is quantified by the ratio of second largest axis to largest axis of the inertia tensor (b/a) and the ratio of the smallest over the largest axis (c/a).

4.4.2   The wall-like environment of CGVs

The CGV-G constellation is quite generic for void halo systems. We find that all 8 void halo configurations are embedded in prominent walls. The void walls have a typical thickness of around $0.4\ h^{-1}\mathrm{Mpc}$. They show a strong coherence and retain the character of a highly flattened structure out to a distance of at least $3\ h^{-1}\mathrm{Mpc}$ at each side of the CGV haloes. Five out of the eight haloes reside in filamentary features embedded within the surrounding walls. Most of these filaments are rather short, not longer than $4\ h^{-1}\mathrm{Mpc}$ in length, and have a diameter of around $0.4\ h^{-1}\mathrm{Mpc}$. Compared to the prominent high-density filaments of the cosmic web on larger scales, void haloes live in very feeble structures.

An additional quantitative impression of the morphology of the typical void halo surroundings may be obtained from Figure 4.13. For haloes CGV-D_a (top) and CGV-G_a (bottom), the figure plots the shape of the spatial distribution of neighbouring haloes larger than $10^8\ h^{-1}\mathrm{M}_\odot$ up to a distance of 3500 $h^{-1}\mathrm{kpc}$. In

both situations we see that for close distances of the halo, out to $< 500 \, h^{-1}$kpc, the distribution of surrounding halo is strongly filamentary ($a > b, c$ and $c/a < b/a <$ $0.1 - 0.15$). Beyond a distance of $\approx 800 \, h^{-1}$kpc, the distribution quickly attains a more flattened geometry, characteristic of a wall-like configuration ($a > b > c$).

In all, we find that the environment of our selected void haloes displays the expected behaviour for structure in underdense void regions. Since Zel'dovich' seminal publication (Zel'dovich 1970), we know that walls are the first structures to emerge in the Universe. Subsequently, mass concentrations in and around the wall tend to contract into filamentary structures. Within the context of structure emerging out of a primordial Gaussian density field, (Pogosyan et al. 1998) observed on purely statistical grounds that infrastructure within underdense regions will retain a predominantly wall-like character. Following the same reasoning, overdense regions would be expected to be predominantly of a filamentary nature, as we indeed observe them to be.

It is reassuring that our analysis of the large scale environment of void haloes appears to be entirely in line with the theoretical expectation of predominantly wall-like intravoid structures. This conclusion is also confirmed by the evolution of the CGV configurations, as we will discuss extensively in section 4.4.4.

4.4.3   Intravoid Filaments

Within the confines of the wall surrounding the CGV-G void halo complex (Figure 4.10, top right-hand frame), we find a large number of thin tenuous filamentary features. A particularly conspicuous property of these tenuous intravoid filaments is that they appear to be stretched and aligned along a principal direction. It evokes the impression of a filigree of thin parallel threads. The principal orientation of the filigree coincides with that of more pronounced filamentary and planar features that span the extent of the void (see Figure 4.1).

The phenomenon of a tenuous filigree of parallel intravoid filaments, stretching along the principal direction of a void, is also a familiar aspect of the mass distribution seen in many recent large scale cosmological computer simulations. An outstanding and well-known example is that of the mass distribution seen in the Millennium simulation (Springel et al. 2005; Park and Lee 2009). The pattern of aligned thin intravoid filaments is a direct manifestation of the large scale tidal force field which so strongly influences the overall dynamics and evolution of low-density regions (see van de Weygaert and Bond 2008; Platen et al. 2008). Because of the restricted density deficit of voids (limited to $\delta > -1$) the structure, shape and intravoid mass distribution are strongly influenced by the surrounding mass distribution (Platen et al. 2008). Often this is dominated by two, or even more, massive clusters at opposite sides of a void. These are usually responsible for most

of the tidal stretching of the contracting features in the voids interior. Given the collective tidal source, we may readily understand the parallel orientation of the intravoid filaments.

The same external tidal force field is also responsible for directing the filaments in the immediate surroundings of the wall. As may be appreciated from the XZ and XY frame in Figure 4.10, the surrounding void filaments tend to direct themselves towards and along the plane of the wall. Besides affecting the anisotropic planar collapse of the wall, the tidal force field is also instrumental in influencing the orientation of mass concentrations in the surroundings. Walls and filaments are the result of the hierarchical assembly of smaller scale filaments and walls. The first stage towards their eventual merging with the large scale environment is the gradual re-orientation of the small scale filaments and walls towards the principal plane or axis of the dominant large scale mass concentration.

While the crowded filigree of tenuous intravoid filaments forms such a characteristic aspect of the dark matter distribution in voids, it is quite unlikely we may observe such filaments in the observed galaxy distribution. Most matter in the universe finds itself in prominent large scale filaments. Filaments with diameters larger than 2 h^{-1}Mpc represent more than 80% of the overall mass and volume content of filament. For walls, 80% of the mass and volume is represented by walls with a thickness larger than 0.9 h^{-1}Mpc (Cautun et. al, in preparation). The large number of low density void filaments will have hardly sufficient matter content to form any sizeable galaxy-sized dark halo.

4.4.4   Evolution of the intravoid cosmic web

The intention of our study is to investigate the possible origin of the VGS_31 system. To this end, we have followed the evolution of the web-like void environment of the eight CGVs.

In Figure 4.14, we display the evolution of CGV-D (left) and CGV-G (right) and their environment. At $z = 0$, both systems are in a very similar configuration, within a clearly defined wall-like environment. In earlier stages of formation, we see a system consisting of a large number of thin filaments. These filaments rapidly merge into a more substantial dark matter filament, which is embedded in a wall-like plane. The tenuous walls and filaments get rapidly drained of their matter content, while they merge with the surrounding peers. By redshift $z = 0.55$, only the most prominent wall remains, aside from a few faint traces of the other sheet-like structures. By that time, the filamentary network is nearly completely confined to the plane of the large wall. Small tenuous filaments have been absorbed by the wall, while the ones within the wall have merged to form ever larger filaments. In the interior of the dominant wall we find the corresponding CGV haloes.
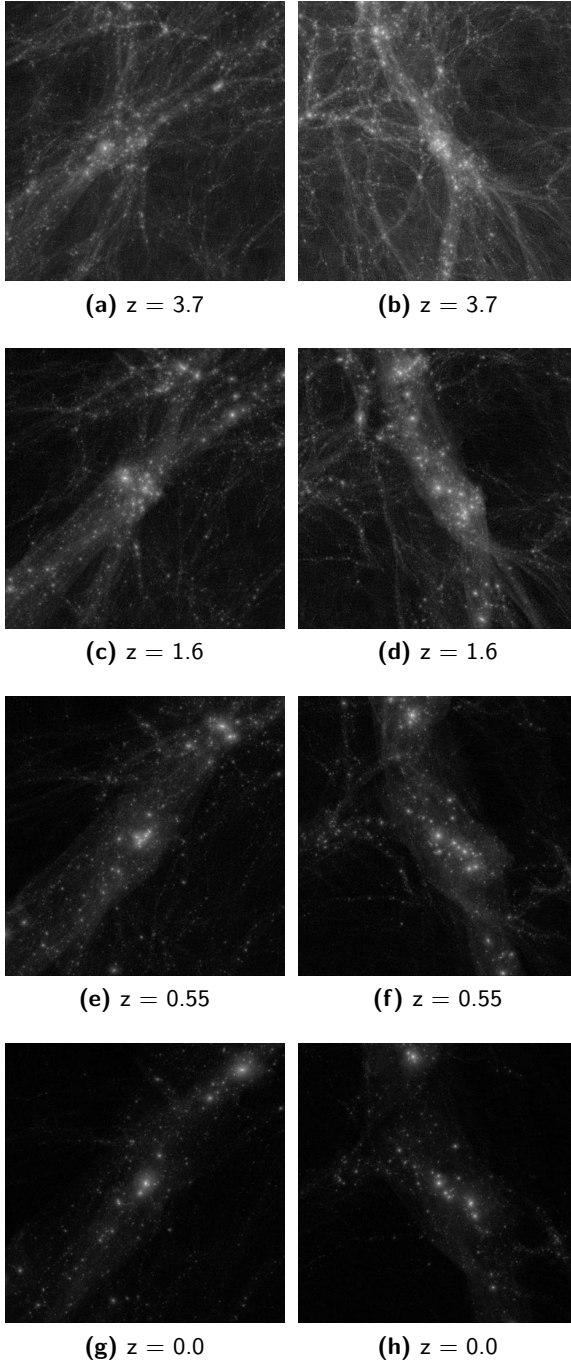
(a) z = 3.7

(b) z = 3.7

(c) z = 1.6

(d) z = 1.6

(e) z = 0.55

(f) z = 0.55

(g) z = 0.0

(h) z = 0.0

Figure 4.14: Evolution of web-like environment of CGV haloes. The density distribution in a box of $2\ h^{-1}\mathrm{Mpc}$ around each halo is shown at four redshifts: $z = 3.7, 1.6, 0.55$ and $z = 0.0$. Left: CGV-D. Right: CGV-G.

Over the most recent 5 billion years, there is very little evolution of the web-like environment of the haloes, with most of the changes being confined to the main sheet. However, there is some variation in time-scale between the different halo configurations. While the CGV-D system has not fully materialized until $z = 0.55$, the CGV-G system is already in place at $z = 1.6$. Interestingly, as we will notice below, this correlates with a substantial difference between the morphological evolution of the surroundings at high redshifts. From early times onward, CGV-G is found to be embedded in a locally prominent wall. CGV-D, on the other hand, finds itself in the midst of a vigorously evolving complex of small-scale walls and filaments that gradually merge and accumulate in more substantial structures (eg. Figure 4.12).

The evolutionary trend of the voids infrastructure is intimately coupled to the dynamics of the evolving mass distribution. Figure 4.15 correlates the density field in and around two central CGV haloes with the corresponding velocity field. To this end, we depict the mass and velocity field in two mutually perpendicular $0.5\ h^{-1}$Mpc slices. The XY plane is the plane of the wall in which the halo is embedded. The YZ plane is the one perpendicular to that and provides a edge-on view of the wall. The vector arrows show the velocity with respect to the bulk velocity of the primary halo.

The wall in which CGV-A is embedded still contains an intricate network of small and thin filaments. Within the wall we observe a strong tendency for mass to flow out of the area centred around the CGV-A haloes. In the XY plane of the wall we recognize stronger motions along the filaments. However, the flow pattern is dominated by the outflow from the sub-voids in the region. The edge-on view of the YZ plane illustrates this clearly, showing the strength of the outflow from the voids below and above the wall. In general, we recognize the outflow in the entire region, inescapably leading to a gradual evacuation from the region and the dissolution of the structural pattern. The mass distribution in the environment of the CGV-D halo has a somewhat different character. It is dominated by the presence of a massive and prominent filament, oriented along the diagonal in the XY-plane. This filament is embedded in a flattened planar mass concentration that also stretches along the filament direction. We clearly observe that the CGV-D halo is participating in a strong shear flows along the filament. The strong migration flow along the filament stands out in the lower part of the YZ plane. In the YZ plane we find it combines with a void outflow out of a large sub-void below the wall, and a weaker outflow out of a less pronounced void above the wall.

Evidently, as matter continues to flow out of the sub-voids and subsequently moves in the walls towards the filaments in their interior and at their boundaries, we will see a gradual dissolution of the intravoid web-like features. In an upcoming
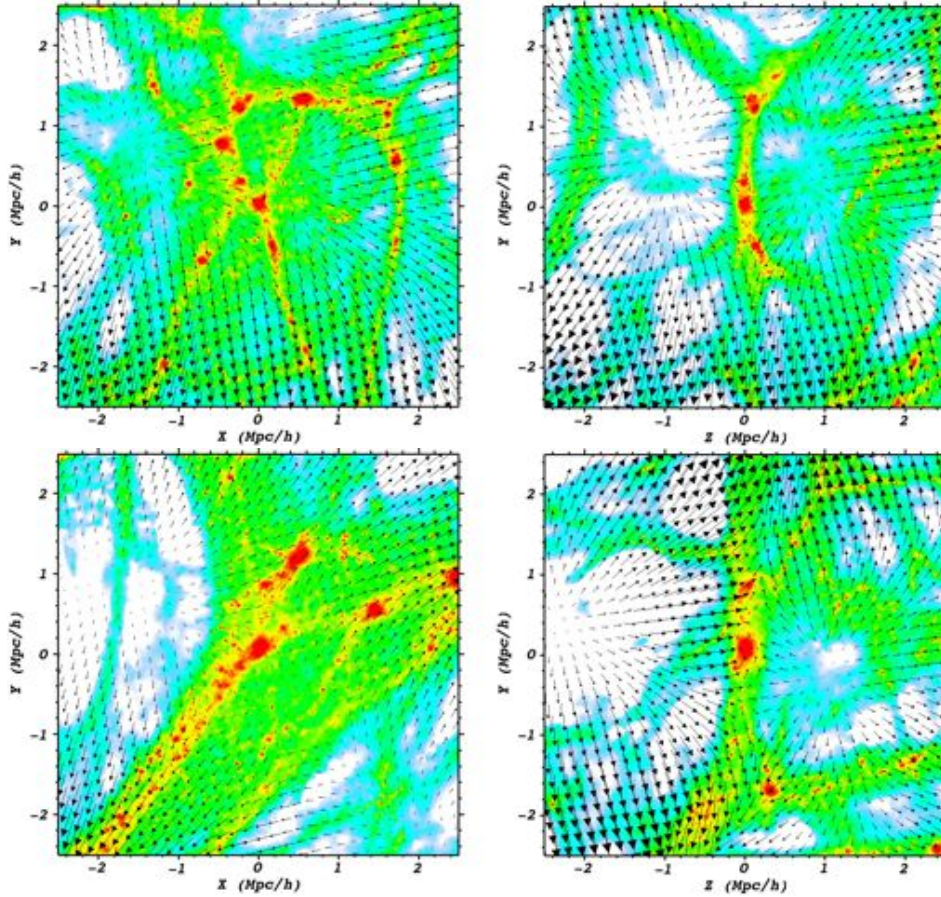
Figure 4.15: Density and velocity field around two central haloes, CGV-A_a and CGV-D_a. The fields are shown in two mutually perpendicular $0.5\,h^{-1}\mathrm{Mpc}$ thick central slices, the central XY plane (left) and the central YZ plane (right). The XY plane is the plane of the wall in which the halo is embedded. The YZ plane is the one perpendicular to that and provides the edge-on view on the wall. The vector arrows show the velocity with respect to the halo bulk velocity. The density levels are the same in each diagram, the length of the vector arrows is scaled to the mean velocity in the region around the halo (and thus differs in top and bottom row).

publication, we will focus in more detail on the dynamics of the walls, filaments and voids.

A more systematic analysis of the structural morphology around the CGV haloes confirms the visual impression of the evolving system of filaments. Particularly telling is the observed evolution of the (Mollweide) sky projection of evolving mass distribution around the CGV haloes. Figure 4.12 shows how the dark matter sky configuration around primary haloes CGV-D_a (left column) and CGV-G_a (right column) evolves from redshift z=3.7 to the present epoch, $z = 0$. In both cases, we recognize a circular ring of matter around the sky, the archetypical signature of the wall-like arrangement of the surrounding mass distribution at high redshifts (z=3.7 and z=1.6).

Towards later times we observe the gradual evacuation of matter out of the main body of the wall, and its accumulation at the two diametrically opposite spots indicating the direction of the filament in which the haloes are located. In other words, the evolutionary sequence reveals the draining of matter from the main plane of the wall towards its dominant filamentary spine. In particular the evolving CGV-D environment provides a nice illustration of how this process is accompanied by a gradual merging of thin tenuous walls and filaments into a dominant planar structure (cf. the distribution at z=1.6 with z=0.55). At $z = 3.7$, we cannot yet recognize a coherent wall. Instead, the "spiderlike" pattern on one hemisphere is that of a plethora of small-scale incoherent planar features that subsequently merge and contract into a solid wall, via an intermediate stage marked by two planar structures (z=1.6). The situation is somewhat different for CGV-G, which even at a high redshift is already embedded in a solid wall marking a coherent circle over the sky projection.

With the help of the NEXUS+ technique, we systematically analyse the evolution of the morphology and composition of the large-scale mass distribution. Figure 4.11 shows the evolution of the filamentary and wall-like network around CGV-G. Proceeding from z=2.4, the central row confirms the dramatic evolution of the wall-like structures around the system. At high redshift the region around the halo is dominated by a large wall, the one we recognized in the Mollweide sky projection of Figure 4.12. Perpendicular to the dominant wall, we find the presence of numerous additional sheets. However, these tend to be very tenuous and rapidly merge with the more prominent wall. The entire planar complex has condensed out by z=1.6. When assessing the evolution of the corresponding filaments, we find that their concentration towards the plane of the wall is keeping pace with the contraction of the major wall. This is clearly borne out by the left-hand column of Figure 4.11, which shows the filamentary features visible at the edge-on orientation of the wall. Within the plane of the wall, on the other hand, we find that
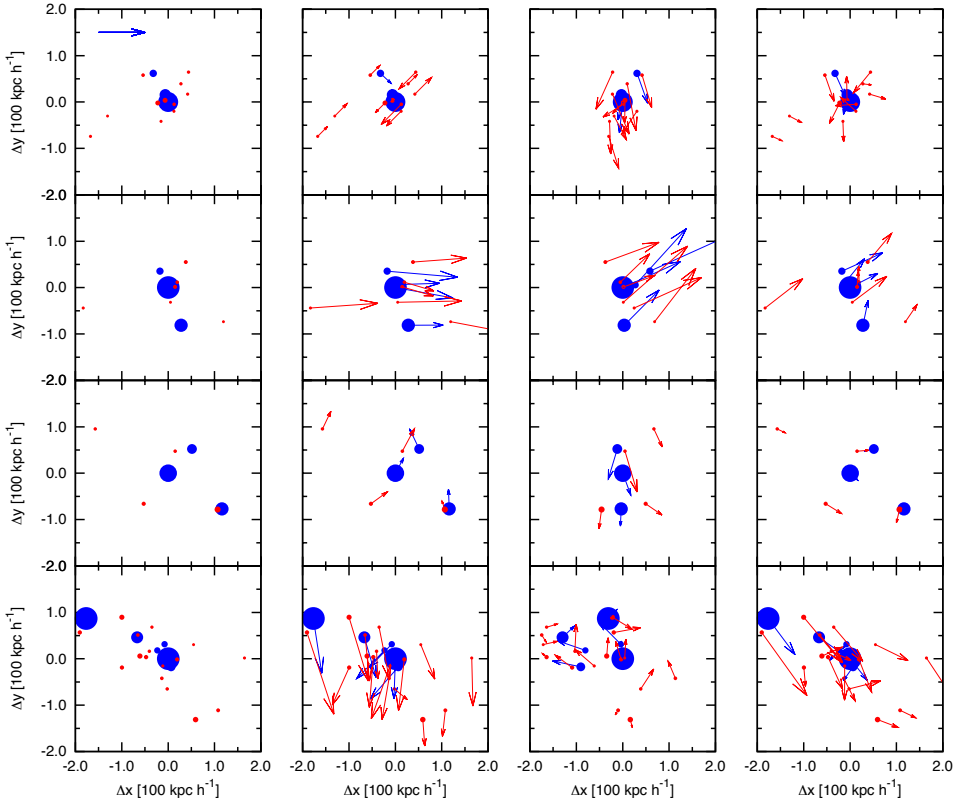
Figure 4.16: CGV haloes and subhaloes: spatial distribution and velocities. The figure shows the spatial distribution, in $200\ h^{-1}$kpc boxes, of haloes and subhaloes, projected onto the plane along the large scale wall in which the systems are embedded. Blue dots: principal haloes with mass $M > 10^9\ h^{-1}\mathrm{M}_\odot$. Red dots: small surrounding haloes with masses between $10^8 < M < 10^9\ h^{-1}\mathrm{M}_\odot$. The size of the dots is proportional to the mass of the haloes. In each row, we show the spatial distribution of the haloes (left), the total peculiar velocity (arrow) of each of the objects (central left), the distribution and total peculiar velocity of each of the objects perpendicular to the wall (central right) and the velocity of the haloes/subhaloes wrt. the centre of mass of the objects (right). We show four systems: CGV-A (top row), CGV-D (second row), CGV-G (third row) and CGV-H (bottom row). The arrow in the top left figure indicates a velocity of $100km/s$.

there is a dynamically evolving system of intra-wall filaments. It defines an intricate network of small filaments at high redshifts, especially prominent in the plane of the large wall and somewhat less pronounced perpendicular to this wall. At later times the filamentary network retracts to only a few pronounced filaments, with the CGV-G system solidly located within the locally dominant filament within the wall. The filaments at later times are especially pronounced at the intersection of two or more walls.

We find that the structural evolution shown in Figure 4.11 is archetypical for all eight void halo systems. All systems begin their evolution in a wall, and within the wall in clearly outlined filaments. By $z = 0.55$, these structures are the only noticeable web-like features left in the immediate surroundings of the haloes. At later times, the morphology of the large scale distribution hardly evolves any more. The principal difference between the eight void systems is their morphological affiliation at later time. At $z = 0$ not all are located in a filament. Some of these systems are exclusively located in the main wall, while others find themselves within a remaining filamentary condensation. In other words, void haloes always find themselves within intravoid walls, but not necessarily within intravoid filaments.

4.5   CGV halo configurations and VGS_31: a comparison

Following our investigation of the CGV void haloes and the intravoid filaments in which they reside, we assess the possible dynamical and evolutionary status of a system like VGS_31 (see section 4.2.2, Beygu et al. (2013)).

A visual inspection of the spatial configuration of haloes and subhaloes in and around the CGVs is presented in Figure 4.16. The blue dots are the principal haloes with mass $M > 10^9 \, \mathrm{M_\odot}$, the red dots are small surrounding haloes whose masses range between $10^8 < M < 10^9 \, \mathrm{M_\odot}$. The location of the primary halo is taken as the origin of the coordinates.

In four halo systems - CGV-D, CGV-E, CGV-G and CGV-H - the principal haloes have arranged themselves in a conspicuous elongated configuration, much resembling the situation of the VGS_31 system. On the other hand, we have not found a configuration consisting of two massive primary haloes accompanied by one or two minor haloes. In this respect, none of the eight CGVs resembles VGS_31. Instead, most systems appear to comprise one dominant principal halo and a few accompanying ones that are less massive.

When considering the distribution of the minor haloes around the CGVs, we find that they tend to follow the spatial pattern defined by the major haloes. The CGV-H system is different: the minor haloes have a much wider and more
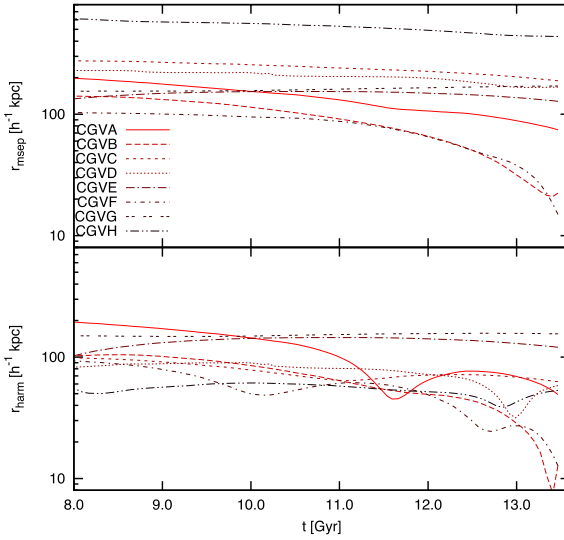
Figure 4.17: Evolution of mean separation (top frame) and harmonic radius (bottom frame) of the CGVs. Plotted are r_{msep} and R_{harm}, in co-moving units, against cosmic time (in Gyr). Each CGV is represented by a different line character, tabulated in the left bottom corner of the top frame.
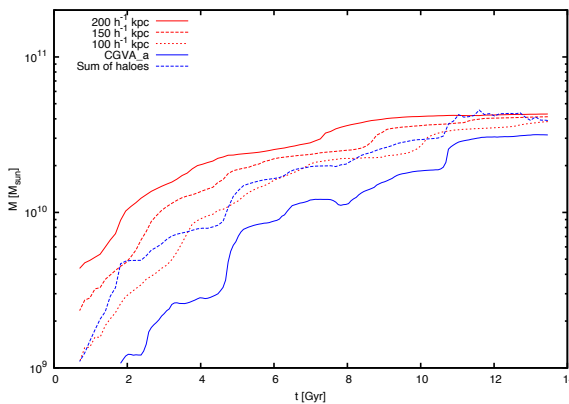

Figure 4.18: Mass growth CGV-A haloes and environment. Plotted are the growth of mass M against cosmic time t. Solid blue line: central CGV-A halo. Dashed blue line: sum of mass in all three CGV-A haloes. Red lines: dark matter mass growth spherical region centred on centre of mass CGV-A system (excluding mass in haloes). Dotted red line: spherical region with radius $100\ h^{-1}\mathrm{kpc}$. Dashed red line: spherical region with radius $150\ h^{-1}\mathrm{kpc}$. Solid red line: spherical region of radius $200\ h^{-1}\mathrm{kpc}$. Note that over the past 3 Gyr, the haloes represent the major share of mass in the region.
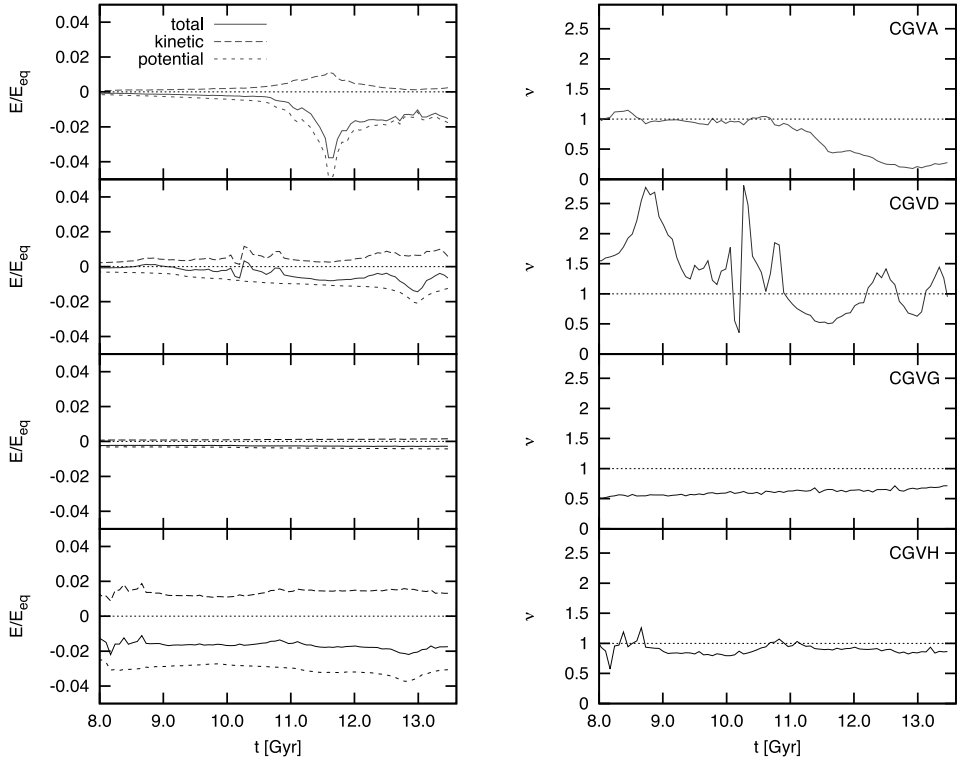
Figure 4.19: Energy of evolving CGV halo systems. Left-hand column: time evolution of "Halo system" kinetic energy, potential energy and total energy (see text for definition). Energy is plotted in units of $E_{eq} = 2 \times 10^{58}$ erg, the potential energy of a 2×10^{12} M$_\odot$ halo. Solid line: total energy E_{tot}. Dashed line: kinetic energy E_{kin}, dotted line: potential energy E_{pot}. Right-hand column: evolution of virial ratio $\mathcal{V}$ (see Equation 4.5). Top row: CGV-A. 2nd row: CGV-D. 3rd row: CGV-G. Bottom row: CGV-H.

random distribution than the more massive ones that are arranged in a filamentary configuration. Overall, however, we do not expect a large number of smaller haloes in the vicinity of these systems.

Part of the systems are moving with a substantial coherent velocity flow along the walls or filaments in which they are embedded. When inspecting the central row of Figure 4.16, we clearly recognize this with the CGV-A and CGV-D systems. Interestingly, they also turn out to be the systems that are undergoing the most active evolution. The latter obviously correlates with a strong evolution of the surrounding mass distribution.

4.5.1 Size evolution of the CGVs

To assess whether the systems have recently formed, we have determined the mean separation and harmonic radius of the CGVs,

$$r_{msep} = \frac{1}{N} \sum_{i,j;i \neq j} |r_{ij}|$$
$$\frac{1}{r_h} = \frac{1}{N} \sum_{i,j;i \neq j} \frac{1}{|r_{ij}|} \tag{4.1}$$

While the mean separation is sensitive to outliers and represents a measure for the overall size of the entire halo system, the harmonic radius of the system quantifies the size of the inner core of the halo system. The evolution of the (co-moving) mean separation and in particular the harmonic radius, shown in Figure 4.17, reflect the gradual contraction of the systems. While CGV-B and CGV-F show a strong contraction over the past 1-2 Gyrs, the overall size of the other systems does not change strongly. This contrasts to the evolution of the core region. As the lower frame of Figure 4.17 shows, in most systems we see a strong and marked evolution over the past 2 to 3 Gyrs, leading to a contraction to a size considerably less than 100 h^{-1}kpc. The haloes in the core will therefore have interacted strongly, involving either infall of small haloes, mergers of major ones and certainly strong tidal influences on each other.

4.5.2 Energy considerations

One of the remaining issues concerns the level to which the haloes of the CGVs are gravitationally bound. In this respect, we should first evaluate the fraction of matter contained in the haloes. Figure 4.18 plots the growth of mass in a region around the central CGV-A halo. The red lines show the developing dark matter mass content in a spherical region of radius 100, 150 and 200 h^{-1}kpc around the

central halo (excluding the mass in the haloes themselves). In addition, the figure plots the halo mass evolution. The solid blue line depicts the growing mass of the central halo, the dashed blue line is the sum of the mass of the three main CGV-A haloes.

As time proceeds, we see that a larger and larger fraction of mass in the environment of the CGV-A system gets absorbed by the haloes. At the current epoch, most of the mass within $100\ h^{-1}$kpc and $150\ h^{-1}$kpc is concentrated in those haloes. Assuming that we may therefore approximate the kinetic and potential energy of the region by that only involving the mass in the haloes, we may get an impression of in how far the halo system is gravitationally bound and tends towards a virial equilibrium.

To this end, we make a rough estimate of the energy content of the halo system. We approximate the kinetic and potential energy by considering each of the haloes as point masses with mass m_i, location $\vec{r}_i$ and velocity $\vec{v}_i$. Note that by doing so we ignore the contribution of the more diffusely distributed dark matter in the same region, which at earlier times is dynamically dominant but gradually decreases in importance (see Figure 4.18). Also, it ignores the contribution of the surrounding mass distribution to the potential energy. The kinetic energy of the system of N CGV haloes, wrt. its centre of mass, is

$$E_K \;=\; \frac{1}{2}\sum_{i=1}^{N} m_i(\vec{v}_i - \vec{v}_{CM})^2\,, \qquad\qquad (4.2)$$

while the potential energy of the system is computed from

$$E_G \;=\; -\sum_{i=1}^{N}\sum_{j=1}^{N}\frac{Gm_i m_j}{|\vec{r}_i - \vec{r}_j|}\,. \qquad\qquad (4.3)$$

In the left-hand column of Figure 4.19 we plot the evolution of the kinetic, potential and total energy,

$$E_{tot} \;=\; E_K + E_G \qquad\qquad (4.4)$$

of four halo systems (CGV-A, CGV-D, CGV-G and CGV-H). The energy is plotted in units of $E_{eq} = 2 \times 10^{58}$ erg, which is approximately the potential energy of 2×10^{12} M$_\odot$ haloes at 1Mpc distance. We see that half of the systems have a rather quiescent evolution. Of these, CGV-H strongly and CGV-H marginally gravitationally bound. A far more interesting and violent evolution of the energy content of the halo systems CGV-A and CGV-D. Both involve an active and violent merger history, marked by a continuous accretion of minor objects and a few

major mergers. In particular the major mergers are accompanied by a strong dip in the potential and binding energy.

To get an impression of the corresponding energy stability, we plot the evolution of the virial ratio,

$$\mathcal{V} = \frac{2E_K}{E_G} \,, \tag{4.5}$$

in the second column of Figure 4.19. For a fully virialised object, $\mathcal{V} = 1$. While the computed $\mathcal{V}$ parameter only provides an impression of the energy state of the systems, it does confirm the impression that CGV-H and CGV-G are halo systems that are in largely in equilibrium. At the same time, the same diagrams for the CGV-A and CGV-D systems reflect their violent history. This appears to continue up to recent times.

4.5.3 The origin of VGS_31

Translating the CGVs to VGS_31, we note that all haloes detected at $z = 0$, are local to their environment. They, and their progenitors, were never further removed than 330 kpc from the main halo. Even if so far removed, we find that the distance between the haloes rapidly decreased at early times. We therefore conclude that the galaxies in VGS_31 originated in the same region, and originally were probably located in the same proto-wall, and possibly even proto-filament. In other words, the galaxies in the VGS_31 system did not meet just recently, but have been relatively close to each other all along their evolution. It answers our question whether VGS_31 might consist of filamentary fragments that only recently assembled.

Moreover, the strong evolution of the several CGV halo cores is an indication for the fact that the two dominant galaxies VGS_31 - VGS_31a and VGS_31b, may recently have undergone strong interactions as indeed their appearance confirms. It would imply that the disturbed nature of the galaxies of VGS_31 is a result of recent interactions between the galaxies. On the other hand, other CGVs had a rather quiescent history. If VGS_31 would correspond to one of these systems, we may not have expected the marks of recent interaction that we see in VGS_31a and VGS_31b.

4.6   Discussion & Conclusions

In this study, we have investigated the formation history of dark matter halo systems resembling the filamentary void galaxy system VGS_31 (Beygu et al. 2013). The VGS_31 system is a 120kpc long elongated configuration of 3 galaxies found

in the Void Galaxy Survey (Kreckel et al. 2011). In the CosmoGrid simulation we looked for systems of dark haloes that would resemble the VGS_31 system. To this end, we invoked a set of five criteria. In total, eight systems were identified, CGV-A to CGV-H.

The 2048^3 particle CosmoGrid simulation has a rather limited volume, $V = 21\ h^{-1}\mathrm{Mpc}^3$, but a very high spatial resolution. While its limited size impedes statistically viable results on large scale clustering as its volume is not representative for the universe, its high mass resolution renders it ideal for high-resolution case studies such as the one described in this study.

While the CosmoGrid simulation is a pure dark matter simulation, a more direct comparison with the HI observations of VGS_31 will have to involve cosmological hydro simulations that include gas, stars, and radiative processes. Nonetheless, as galaxies will form in the larger dark matter haloes and gaseous filaments will coincide with the more substantial dark matter filaments, our study provides a good impression of the expected galaxy configurations in voids. Nonetheless, it is good to realize that most of the intricate structure seen in our simulations would contain too small amounts of gas to be observed.

For each of the CGVs we examined the formation history, the merging tree, and the morphology of the large scale environment. In our presentation, we focus on the two systems that represent the extremes of the VGS_31 resembling halo configurations. System CGV-G formed very early in the simulation and remained virtually unchanged over the past 10 Gyr. CGV-D, on the other hand, formed only recently and has been undergoing mergers even until $z = 0$.

We find that all CGVs are located in prominent intra-void walls, whose thickness is in the order of $0.4\ h^{-1}\mathrm{Mpc}$. Five halo complexes are located within filaments embedded in the intra-void wall. In all situations the filamentary features had formed early on, and were largely in place at $z \approx 1.6$. These intra-void filaments are short and thin, with lengths less than $4\ h^{-1}\mathrm{Mpc}$ and diameters of $\sim 0.4\ h^{-1}\mathrm{Mpc}$.

The spatial distribution of dark matter haloes resembles that of the dark matter. We see the same hybrid filament-wall configuration as observed in the dark matter distribution. Close to the main halo, within a distance smaller than $700\ h^{-1}\mathrm{kpc}$, the neighbouring haloes are predominantly distributed along a filament. On larger scales, up to $\approx 3.5\ h^{-1}\mathrm{Mpc}$, the haloes are located in a flattened wall-like structure.

In addition to our focus on the evolving dark matter halo configurations, we also studied the morphology and evolution of the intricate filament-wall network in voids. Our study shows the prominence of walls in the typical void infrastructure. Unlike the larger scale overdense filaments, intra-void filament are far less outstanding with respect to the walls in which they are embedded.

What about VGS_31? Our study implies it belongs to a group of galaxies that was formed in the same (proto)filament and has undergone a rather active life over the last few Gigayears. The galaxies in the VGS_31 system did not meet just recently, but have been relatively close to each other all along their evolution. We also find that it is unlikely for VGS_31 to have many smaller haloes in its vicinity. The fact that we find quite a diversity amongst the CGVs also indicates that VGS_31 may not be typical for groups of galaxies in voids.

Acknowledgements